Approach to Control Permittivity and Shape of Centimeter-Sized Additive Manufactured Objects: Application to Microwave Scattering Experiments

H. Saleh, H. Tortel, C. Leroux, A. Coudreuse, A. Litman, J.-M. Geffrin

HAL Id: hal-02978730

https://hal.science/hal-02978730

Submitted on 25 Feb 2022

Approach to Control Permittivity and Shape of Centimeter-Sized Additive Manufactured Objects: Application to Microwave Scattering Experiments

H. Saleh, H. Tortel, C. Leroux, A. Coudreuse, A. Litman, J.-M. Geffrin

Abstract— Controlling the electromagnetic properties of dielectric objects is demanded in microwave applications such as radar cross section studies, metamaterial design and antennas prototyping. Additive manufacturing has made the fabrication of desired shapes easier, but there is still room for improvement in controlling the permittivity. This paper proposes a novel approach to control the permittivity of 3D printed objects, in particular the ones with low permittivity contrasts. The effective permittivity is set by locally varying the material density. The object is first meshed using tetrahedral meshing software. Then its air percentage is controlled by adjusting the diameter of cylinders, which are positioned at each edge of the mesh. By tuning the volume fraction, one can achieve the required effective permittivity. Design, manufacturing and characterization steps are discussed while considering the specific case of spheres. With such a canonical shape, the effective permittivity can be directly retrieved by comparing far field electromagnetic scattering measurements with Mie computations. Bistatic Radar Cross Section measurements and simulations are provided and discussed. They enable us to assess the validity of the proposed methodology, in particular the good adequacy between the adequately chosen unstructured air/material distribution, the desired relative permittivity and the good homogenization of the object.

Index Terms—Additive manufacturing, 3D printing, permittivity control, low permittivity, scattering, anechoic chamber, microwave analogy, RCS, homogeneization

I. INTRODUCTION

ADDITIVE manufacturing is nowadays widely implemented in the fields of communication and imaging, ranging from lightweight electronic devices for aerospace applications to antennas and RF components for wireless communications. It offers the opportunity to accurately construct complex-shaped objects and to combine different types of materials such as metals, polymers, ceramics and composites, thus enlarging the range of attainable permittivity values. 3D printing has become helpful in the fabrication of gradient index dielectric or metal/dielectric periodic substrates, in particular by making subwavelength structuration in the printed material.

Several examples of such developments have been proposed to design Luneburg lenses using different types of geometries and materials, such as cubical lattice from ceramic [1], discrete polymer cubes [2], or polycarbonate associated with space-filling curves [3]. A woodpile structure of polymer was also designed as an electromagnetic bandgap material [4]. Additive manufacturing of polycarbonate acrylonitrile butadiene styrene (ABS) was used for the manufacturing of spatially variant self-collimation lattice for arbitrary waves distribution inside a structure [5], as well as for the manufacturing of a uniaxial anisotropic rectangular metamaterial [6]. In [7], a metal-dielectric-metal gradient phase partially reflecting surface has been manufactured for antenna beams steering by creating air holes of different dimensions. In [8] a study is made on the microwave dielectric properties of ABS/Barium titanate (BaTiO3) composites in fused deposition modeling 3D printing. In particular, relative permittivity measurements of ABS/BaTiO3 composites with different weight percentages of BaTiO3 have been made. In [9] a woodpile structure has been proposed to realize a three-dimensional electromagnetic concentrator by Stereolithography process. Complex 3D periodic structures and millimeter wave antennas and bandpass waveguides have been fabricated through ceramic stereolithography with materials like Zirconia and Alumina for their high dielectric constant ($\varepsilon'>7$) and low losses (ε'' close to 0) [10-13].

Nevertheless, very few of those objects, after being shaped and printed, have been characterized over a wide frequency range. Indeed, the characterization is often performed at a single frequency. Let us nevertheless mention [3] where interesting efforts have been made to characterize the permittivity of plates over a wide frequency range, while assessing their polarization sensitivity by rotating the sample. As well, some of the aforementioned references only describe computations with no associated actual realizations which could serve as a full proof of concept.

In our targeted applications, as discussed hereafter, objects

have often quite peculiar shapes. These shapes as well as their associated permittivities, need to be controlled on demand. For this reason, a new approach to printable effective medium is developed in this paper. The proposed method has been designed to facilitate the assignment (almost in a systematic way) of a desired permittivity value to any shape generated by any Computer Aided Design (CAD) software.

The motivation for this research derives from the microwave analogy [14], whose principle is to scale electromagnetic scattering experiments from optics/UHF band to microwaves by enlarging/reducing both the target's size and the incident wavelength by the same factor, while conserving the same permittivity, permeability and shape. In our previous studies, machining or additive manufacturing of bulk materials has been used to fabricate analogues (with same shapes and electromagnetic properties as the unscaled objects) with real part of relative permittivity between 3 and 15 [15, 16]. An interest has been shown recently toward the manufacturing of analogs with low permittivity (between 1 and 3) to mimic the electromagnetic response of photosynthetic microalgae particles. In [17] this question has been investigated on analogs of spheroidal particles machined from rigid polyurethane foams with permittivities ranging from 1.3 to 1.45. Due to machining difficulties and a request for lower prmittivity, we have been led to derive a simple and "user friendly" method capable of producing objects of any shape and size while controlling their permittivity spatial distribution in a one-shot manufacturing process.

Our choice was to start from a non-structured organization of the material that can be obtained with any meshing software when automatically meshing the object under test in a conformed way. We then control the electromagnetic properties of the objects to be constructed via additive manufacturing technologies, by adapting their internal volume fractions. Indeed, we replace the internal infinitely thin edges generated by the meshing software with cylinders of varying diameters thanks to a CAD process. We also pay special attention to conserve an effective isotropy in the resulting medium, which is compulsory for our microwave analogy applications. By introducing multiple voids, we can manufacture objects with relative permittivity ranging between 1 and 3.

The article is organized as follows. In Section II, the proposed manufacturing process is carefully detailed. Examples of manufactured spheres with different meshes and inner cylinders are displayed, and their permittivity are estimated from Radar Cross Section (RCS) measurements performed in the anechoic chamber of the Centre Commun de Recherches en Microondes (CCRM) and compared in the 2 to 18 GHz frequency band. In Section III, the RCS measurement experimental facility is described as well as the complex permittivity estimation protocol. Comparisons of scattered fields are presented, and uncertainties are discussed. A conclusion follows.

II. VARYING THE EFFECTIVE PERMITTIVITY

A. Volume fraction control

The main idea of our manufacturing process is to control the permittivity by adjusting the volume fraction of the material in a quasi-systematic way, without much intervention from the end-user. By doing so, the permittivity could thus be set to any value between the lower limit (which is slightly above 1) and the upper limit (which is the permittivity of the printer's bulk resin and is reached when there are no voids in the object).

First, from the permittivity of the bulk material used by the 3D printer, a pre-estimation of the needed volume fraction can be made using a simple Maxwell-Garnet approximation. Second, voids inside the objects are created. In this step appears one of the benefits of the technique we propose. Indeed, voids have to be small enough to consider that the resulting medium is homogeneous at the highest working frequency (which is often considered to be a tenth of the wavelength in EM simulation softwares). Starting from the CAD file of the object to be built, a standard meshing software is used to discretize the inner structures of the object with a tetrahedral mesh. The settings of the meshing software are such that the tetrahedras are sized as identically as possible. The new meshed geometry of the object is then saved in a ".msh" format file containing the coordinates of all the nodes and edges. The edges are then replaced with cylinders. The overall air/solid volume fraction is then controlled through the choice of the cylinders diameters. The latter are chosen in a way to adjust the total material density to the value obtained from the Maxwell-Garnett estimation. The entire methodology is summarized in Fig. 1.
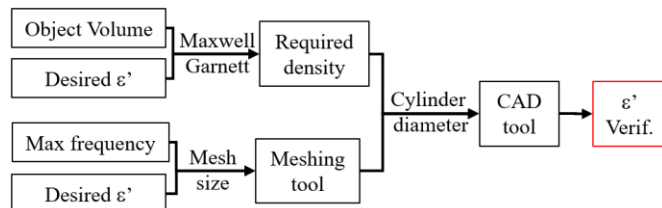

Fig. 1. Input parameters to the CAD tool based on the object' volume, desired permittivity and maximum working frequency.

B. Preparing 3D printing

The different process steps, from meshing to fabrication, are summarized in the example in Fig. 2. First, the geometry is designed, then it is meshed into tetrahedras using, in our case, the free meshing software "Gmsh" [18] (Fig. 2-a). The meshing yields the positions of the nodes and the connecting edges. The edge connections between the nodes are then replaced by actual cylinders. In our work, the creation of the cylinder was achieved by using the commercial software CATIA [19] where the user sets the desired cylinder's diameter value in a macro script that automatically transforms the edges into cylinders (Fig. 2-b). The cylinders generation could also be done using any other CAD software (in an ongoing project it is being made with MATLAB). Once the cylinders are created, a CAD file (".stl") is generated and

processed by a slicer used to generate the layers that will be printed (Fig. 2-c). Those layers are then built one after the other by the 3D printer (Fig. 2-d).
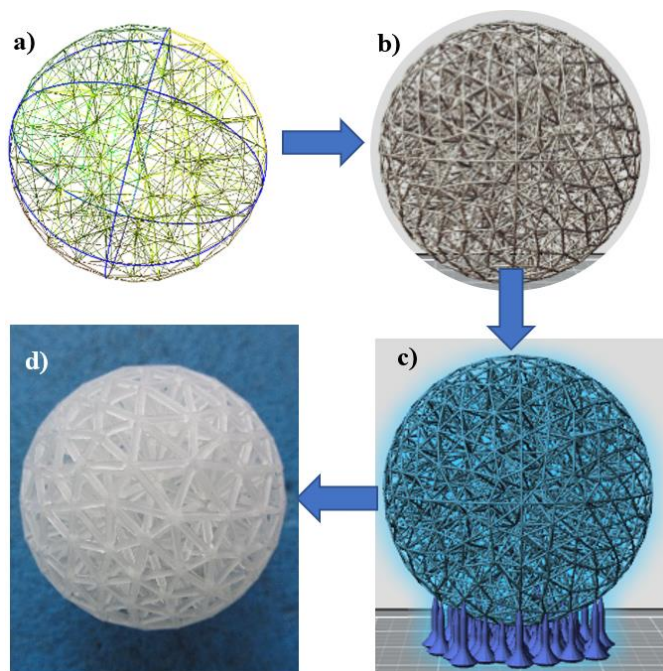

Fig. 2. Fabrication steps and porosity control using meshed geometries: a) creating the meshing of the object, b) generating the cylinders, c) preparing the file for the printer, d) manufacturing the object

Note that the mesh can be created to accommodate different sub-domains in a given object, and the cylinder diameters can be adjusted independently in each sub-domain to change the internal permittivity, or to create permittivity gradients.

In practice, the 3D printer we used is based on the DLP (Digital Light Processing) technology: a photosensitive resin is polymerized layer by layer from the bottom to the top of a tank containing the liquid resin. At each layer, a mask using micromirror matrix is applied and determines at each layer surfaces to be polymerized or not. The support is then pulled up and layers are created ones after the others. The photosensitive resin used by this additive manufacturing printer is an acrylate-based formulation. The light used is in the visible band (405 nm). The thickness of every photo-polymerized layer is 50 μm. Its permittivity has been determined with an average value of $2.91 + j0.13$ in the working frequency range (see Section III for more details about the permittivity estimation procedure). An example of a printed sphere, with conformal meshing, is shown in Fig. 3.
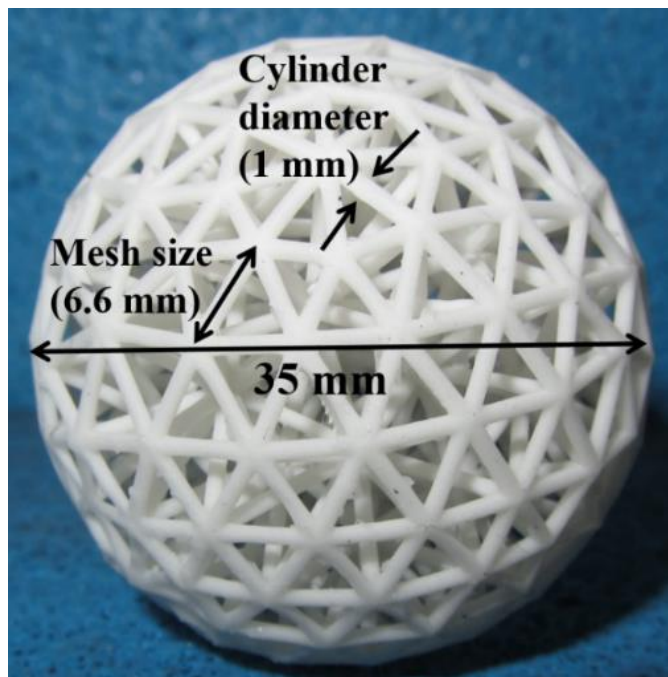

Fig. 3. Photography of a 35 mm diameter sphere made with 804 cylinders each of 6.6 mm length and 1 mm diameter.

The technique was tested on different spheres with different permittivity values ranging between 1 and 3. Indeed, in our targeted application (microwave analogy), low permittivities are of special interest. Due to the low permittivity required and to ensure a better mechanical robustness of the resulting object, we favored tetrahedral meshes to square lattices. We have also taken great care to come up with a procedure which generates quasi-randomly oriented cylinders inside the object mimicking as best as possible a homogeneous equivalent medium. Another important request of our scattering applications is that the resulting effective medium should not be sensitive to the angle of incidence of the incoming wave or to its polarization. To verify that this isotropy is achieved in practice, all the permittivity estimations were made at four different orientations of the target. The last parameter that can be tuned is the length of the cylinders, and it is simply set in the meshing software. It is supposed that the smaller the cylinders length, the better the homogenization.

C. 3D printing of spheres with low permittivity

For each manufactured sphere, the obtained permittivities have been carefully investigated in orientation, polarization and frequency (see Section III for a detailed description of the scattering measurement setup and the permittivity estimation procedure).

The retrieved parameters of the low permittivity spheres that have been 3D printed are summarized in Table I. The subscripts in the sphere's names indicate the expected permittivity. This permittivity value was used in our first estimation of the volume fraction to determine the cylinders diameter. The ε'_{MG} stands also for the Maxwell-Garnett estimation of the permittivity but this value was determined after the sphere has been manufactured by comparing the weight of the real object to that of a sphere of the same

diameter but made only with the bulk material (which leads to a first small difference with the expected value). In the last line of the table, ε' is the mean value of the characterized permittivity (average value of all the permittivities estimated from 3 to 17 GHz measurements and over four orientations of the spheres, equivalently corresponding to four angles of incidence for the impinging wave).

Table I. Properties of the lower permittivity spheres: ε<1.5 (λ_{min} is the wavelength in air at 18 GHz). See Table II for higher permittivity spheres

Sphere name	$S_{1.52}$	$S_{1.39}$	$S_{1.23}$	$S_{1.03}$
Mesh size (λ_{min})	1/10	1/2	1/3	1/3
Cylinder diam. (mm)	0.35	1	0.56	0.2
Mass (g)	6.64	5.32	2.71	0.33
ε'_{MG}	1.46	1.35	1.19	1.04
Mean meas. ε'	1.36	1.25	1.13	1.03
$\Delta\varepsilon'/\varepsilon'$	3 %	3 %	3 %	1 %

From Table I, one can see that the measured permittivity is often close to its expected value, even if slightly lower. One can also see that the relative error in the permittivity estimation is rather good. This preliminary estimation may be improved with a full EM computation of the real structure, contained in the ".stl" file. Nevertheless, we decided not to perform such a computation for the main following reason: the manufactured geometry and the computational geometry will never be fully identical. Indeed, additive manufacturing has its own uncertainties as the 3D objects consist of a stack of discrete slices which will depend on the resolution of the 3D printer. Within the used slicer software, there is also no access to the material volume of the resulting object.

This is why we have chosen instead to monitor the weight of the targets to make sure that the quantity of polymerized acrylic used by the machine is actually the one used in the calculation of the permittivity.

D. 3D printing of spheres with high permittivity

As shown previously, the lowest permittivity value that could be obtained and measured is close to 1.02, partially due to the printer resolution and to our scattering measurement level of sensitivity (see Section III.D and in particular Fig. 9 for more insights). The highest achievable permittivity is theoretically the permittivity of the bulk material, which has a real part of 2.91. In practice, there is a gap between the highest achievable permittivity value and the bulk permittivity value. Indeed, permittivities slightly below the bulk permittivity value are difficult to achieve with a DLP technology since they require quite a low air/volume fraction, and therefore the very narrow air holes prevent the liquid resin to flow out of the object after fabrication. This constraint should not occur, for instance, with fused deposition modeling technologies.

Four similar spheres with the same high permittivity value of 2.5 have been designed and manufactured. However, they have been made with various combinations of mesh size/cylinder lengths. Their characteristics are presented in Table II. Again, the subscripts in the sphere's names indicate the expected permittivity. The superscript represents the

cylinders diameter.

Table II. Properties of 4 spheres having a permittivity close to 2.5 and a diameter of 35 mm (λ_{min} is the wavelength in air at 18 GHz) but made with different cylinder lengths and diameters.

Sphere name	$S_{2.5}^{2.5}$	$S_{2.5}^{1.3}$	$S_{2.5}^{1.15}$	$S_{2.5}^{1}$
Mesh size	$\lambda_{min}/3$	$\lambda_{min}/6$	$\lambda_{min}/7$	$\lambda_{min}/8$
Cylinder diam. (mm)	2.5	1.3	1.15	1
Mass (g)	24.41	23.56	22.55	24.39
ε'_{MG}	2.44	2.53	2.49	2.62
Mean measured ε'	2.39	2.40	2.35	2.51
$\Delta\varepsilon'/\varepsilon'$	6 %	7 %	5 %	6 %

As with the low permittivity spheres, for each sphere of Table II, the measured permittivity is close to the expected value. The relative error is slightly larger than for the low permittivity spheres but is still satisfactory. Apart from the $S_{2.5}^{1}$ sphere, the measured permittivities are slightly lower than the expected values. When pushed to the limits, as with the $S_{2.5}^{1}$ sphere, the different cylinders lengths/diameters combinations might impact the inhomogeneity of the material and therefore the retrieved permittivity.

E. Frequency, sphere orientation and cylinder dimensions influences

As it can be seen in Fig. 4, for the low permittivity spheres, the measured permittivities are almost identical for the four orientations of the spheres. Moreover, they do not show any real variation with respect to the frequency, despite an expectable slow decreasing behavior (probably inherent to the acrylate resin itself as it can be seen in Fig. 7). Such a behavior is not encountered with the higher permittivity sphere $S_{2.5}^{1.15}$ as it presents some variations with the frequency. Since the cylinder length is $\lambda_{min}/7$, the air voids are quite small and therefore the observed oscillations were not expected.
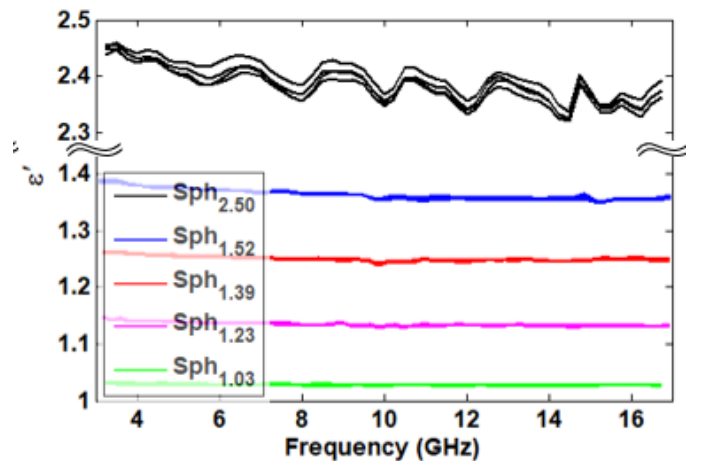

Fig. 4. Real part of the relative permittivity of the meshed spheres presented in Table I as a function of the frequency. For the sake of comparison, the results obtained with a higher index sphere $S_{2.5}^{1.15}$ (presented in Table II) are also shown. For each sphere, 4 permittivity determinations are made, corresponding to 4 orientations of the sphere.

Fig. 5 shows the evolution along the frequency of the measured permittivity of the spheres described in Table II. As

it can be seen, each permittivity is almost well reproduced whatever the orientation of the sphere. However, with the first sphere ($S_{2.5}^{2.5}$), the oscillations in the measured permittivity as a function of the frequency are large. This was due to the relatively long cylinders (cylinders lengths equal to $\lambda_{min}/3$). The idea was then to reduce the lengths of the cylinders in order to reduce those oscillations. The mesh size has been reduced down to $\lambda_{min}/8$, and the corresponding sphere has then been constructed with 1 mm diameter cylinders. Unexpectedly, the measured permittivity became a bit higher than the intended one. Some differences with respect to the orientations can also be seen.

We supposed that some non-polymerized resin might have been left inside the sphere. This has been confirmed by measuring the weight of the sphere that was nearly 5% higher than expected. This also leads to a higher equivalent permittivity and a behavior that seems more orientation dependent. The $\lambda_{min}/7$ cylinders length made the liquid resin removable, but some oscillations were still visible on the permittivity curve (Fig. 5). That means that there is a tradeoff to find between the tolerated permittivity variations as a function of the frequency, on the one hand, and the highest achievable permittivity value on the other hand.
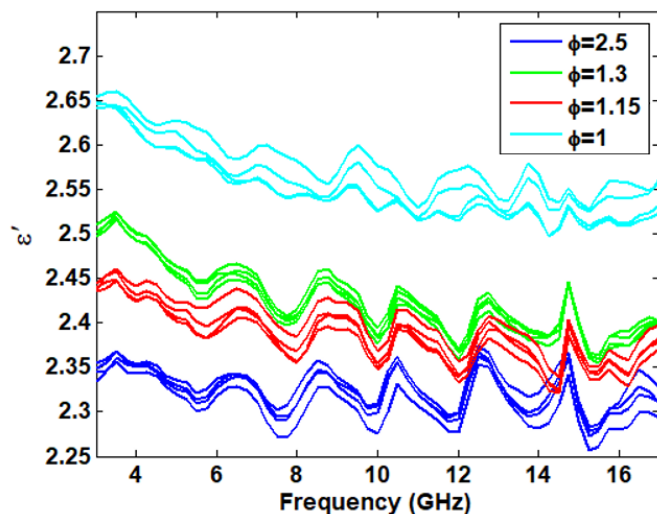

Fig. 5. Real part of the relative permittivity of the 4 spheres presented in Table II as a function of the frequency. For each sphere, 4 permittivity determinations are made, corresponding to the 4 orientations of the sphere. ϕ=2.5 mm is for $S_{2.5}^{2.5}$, ϕ=1.3 mm is for $S_{2.5}^{1.3}$, ϕ=1.15 mm is for $S_{2.5}^{1.15}$, ϕ=1 mm is for $S_{2.5}^{1}$.

We emphasis on the fact that controlling permittivity through additive manufacturing processes is, in general, vulnerable to such kind of phenomena. There would always be a certain difference, due to fabrication, between the 3D model and the manufactured object. Second, the effective permittivities are obtained by locally shaping the material inside the object, and this has unavoidable limitations. Our aim here is to present the limitations of the proposed technique, so that users could be aware of the existing challenges.

III. MEASUREMENT PROTOCOL

In the microwave domain numerous methods have been proposed to measure the permittivity: resonators, cavities, transmission line using coaxial cells and rectangular waveguides. In this work, far field scattering measurements are used to determine the relative permittivity of spherically shaped objects, following the method explained in [20].

A. Experimental set-up

The RCS scattering measurements of the investigated spheres are performed in the anechoic chamber of the CCRM (Fig. 6).The experimental setup has been described in several articles [21, 22]. For this work, the measurements are made in a bistatic azimuthal configuration, nevertheless, other type of configurations such as spherical bistatic or quasi-monostatic are achievable if needed. A transmitting horn antenna placed at a fixed position in far-field illuminates the target (the sphere here). This target is positioned at the center of the measurement setup on a vertical expanded polystyrene mast whose interaction with the target is neglected. It is worth mentioning that the sphere vertical orientation is completely arbitrary with respect to the way the 3D printing slices are constructed. Thanks to the rotation of the mast, the target entirely rotates on itself (360°). This is an interesting feature that allows us to measure each sphere with different orientations to evaluate its homogeneity. A receiving horn antenna also moves circularly around the target to capture the electromagnetic signal, with a total angular excursion of 260°. The transmitting and receiving horn antennas are situated at approximately 1.7 m from the sphere sample.
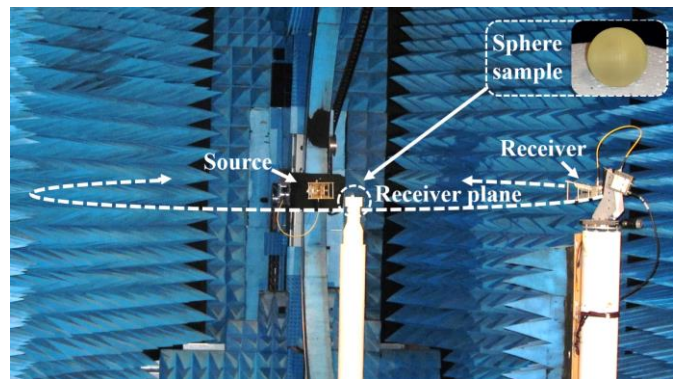

Fig. 6. Sphere under test placed at the center of the circular experimental setup on a vertical expanded polystyrene mast.

The VV polarization case is used in the current study, i.e. the electric fields vectors of both the transmitted and the received signals are perpendicular to the azimuthal plane containing the source, the target and the receiver's trajectory. With such a setup, the signal is measured in both magnitude and phase which allows us to obtain the complex value of the electric field. The scattered electric field E_{sca} cannot be acquired in a unique step, but it is deduced from the complex subtraction of two different measurements: the electric field measured with the sphere on the mast (the total field) and the electric field measured without the sphere (the incident field).

After obtaining the scattered field, a drift-correction procedure is applied [23] to remove the drift errors that could have happened due to the time delay between the total and incident fields measurements. Afterwards, the drift corrected scattered field is calibrated, using the measurement of a reference target, to refer the incident field to a field with magnitude equal to one and a null phase at the target's center. This calibration is of great importance. Indeed, when the measurement and the electromagnetic simulation the same reference point, it becomes possible to compare them quantitatively.

B. Permittivity estimation procedure

To estimate the permittivity, we take advantage of the spherical shape of the sphere. Indeed, in that free space case, if we further assume that the sphere is isotropic and non-magnetic, its scattered field will only depend on the following parameters: the wave frequency, the sphere's radius, its position and its complex permittivity.

In the present case, the sphere's diameter, center position and the frequency are controlled. Moreover, as the antennas are in far-field and as the sphere is not too large with respect to the wavelength, we can assume that the incident field can be modelled as a local plane wave in the vicinity of the sphere. In that case, the field scattered by the sphere can be analytically calculated with Mie series [24], avoiding supplementary model errors. The only missing input element for the simulation is the complex relative permittivity of the sphere.

This permittivity is therefore estimated by minimizing the discrepancy between the measured scattered field and the Mie computation for each frequency independently (using for the sphere diameter the one of the smallest sphere enclosing all the material, *i.e.* 35 mm plus a cylinder diameter).

C. Permittivity measurements

For each object, the scattered fields were measured over the full angular range available by the receiver. This measurement has been repeated for four orientations of the object, taking advantage of the rotation of the mast. The permittivities have been characterized at each orientation and at each frequency. A bulk sphere of 35 mm diameter was manufactured with the same printer used to manufacture all the spheres presented in this paper. That sphere was used to determine the relative permittivity of the bulk material. The mean value obtained over the frequencies is $\varepsilon = 2.91 + j0.13$. Fig. 7 shows in more details the permittivity variations as a function of the frequency and the orientations. The small permittivity fluctuations are directly correlated with the SNR level.
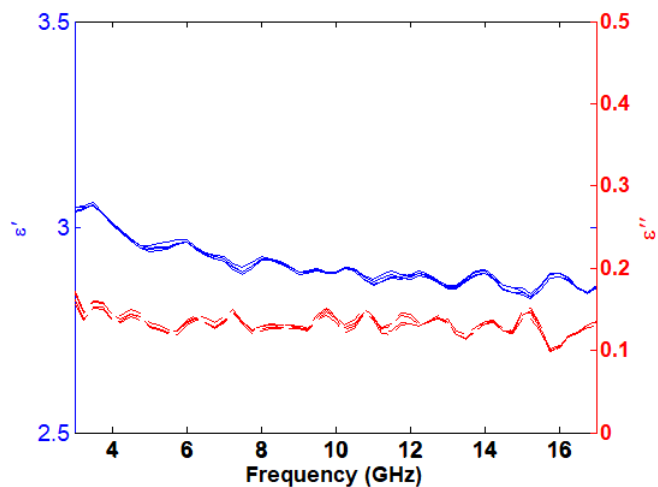

Fig.7. Permittivity of the bulk material determined from the measurements of a 35 mm diameter solid sphere made of acrylate material via additive manufacturing. Estimated real (solid blue lines, left axis) and imaginary parts (dashed red lines, right axis) of the permittivity (for four orientations of the sphere) as a function of the frequency.

D. Scattered field measurements

A comparison at 12 GHz between the measured scattered fields and the simulated ones for the $S_{2.5}^{1.15}$ sphere is shown in Fig. 8. Four different experimental scattered fields are plotted, and they correspond to measurements at four different rotational orientations of the sphere, with an angular step of 90°. The simulation is obtained with Mie theory and it corresponds to a homogeneous sphere of 35 mm diameter having the same relative permittivity value as the one plotted in Fig. 7. A very good agreement between simulation and measurement can be observed, even at the angular regions where the magnitude is quite low (-60 dB and below) and the discrepancies between the different experimental scattered fields are small.
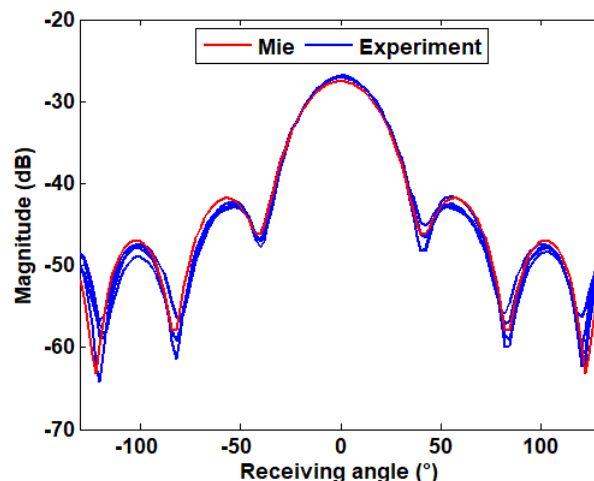

Fig. 8. Magnitudes of the measured fields scattered by the 35 mm diameter meshed sphere $S_{2.5}^{1.15}$ with comparison to the Mie simulation of an equivalent homogeneous sphere of permittivity 2.35+j0.09 at 12 GHz
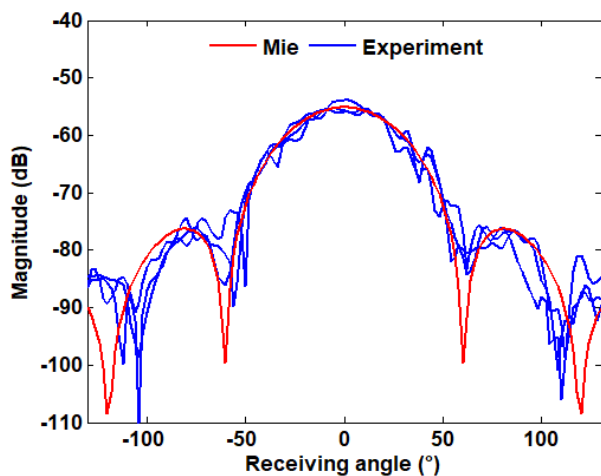
Fig 9. Magnitudes of the measured fields scattered by the 35 mm diameter meshed sphere $S_{1.03}$ with comparison to the Mie simulation of an equivalent homogeneous sphere of permittivity 1.03+j0.002 at 12 GHz.

For $S_{1.03}$, the noise affecting the measurements is more prominent since this sphere is a very low scatterer due to its low permittivity. Despite this noise, as shown in Fig. 9, a good agreement is achieved especially in the forward scattering region (around 0°). The magnitude of the scattered field reaches very low values down to -100 dB as shown on the simulation plots. From an experimental point of view, it is difficult to measure fields with magnitude below -80 dB. Still, at magnitude above -80 dB, the experimental scattered fields follow the same angular variation in magnitude and phase as the simulated ones. These results reflect, on the one hand, our ability to measure low permittivity values that moreover correspond to the predicted values. They also demonstrate our ability to measure fields with low amplitude. This has been made possible thanks to the careful optimization of the measurement setup that we have performed throughout the years [25].

E. Repeatability assessment

To evaluate the accuracy of the measurement and of the permittivity estimation, different types of measurement repeatability assessments have been made (Fig. 10). The measurements are realized at different sphere's orientations. This is done to ensure that the permittivity does not depend on the sphere's orientation. In addition, an evaluation of the measurement uncertainties is made. First, at each position of the receiving angular position (from -180° to 180°), the measurement of the received signal is repeated with 500 acquisitions. The standard deviation of those 500 measurement points is calculated and is considered as the random noise contribution. It is then introduced in the representation of the scattered field to determine the measurement uncertainties (cyan zone in Fig. 10). Second, for each determined permittivity, the minimum and maximum permittivity values as a function of the frequency are selected. Between these two extreme values, 500 permittivity values are randomly selected, and a Mie simulation is run for each of them to obtain all the corresponding scattered electric fields (light red zone). Even for the lower permittivity value case,

the consistency between measurements, noise evaluation, permittivity and its uncertainty, appears to be satisfactory. Almost at every receiving angle, there is a non-null intersection between the measurement uncertainty (cyan zone) and the field resulting from the permittivity estimation uncertainty (light red zones).
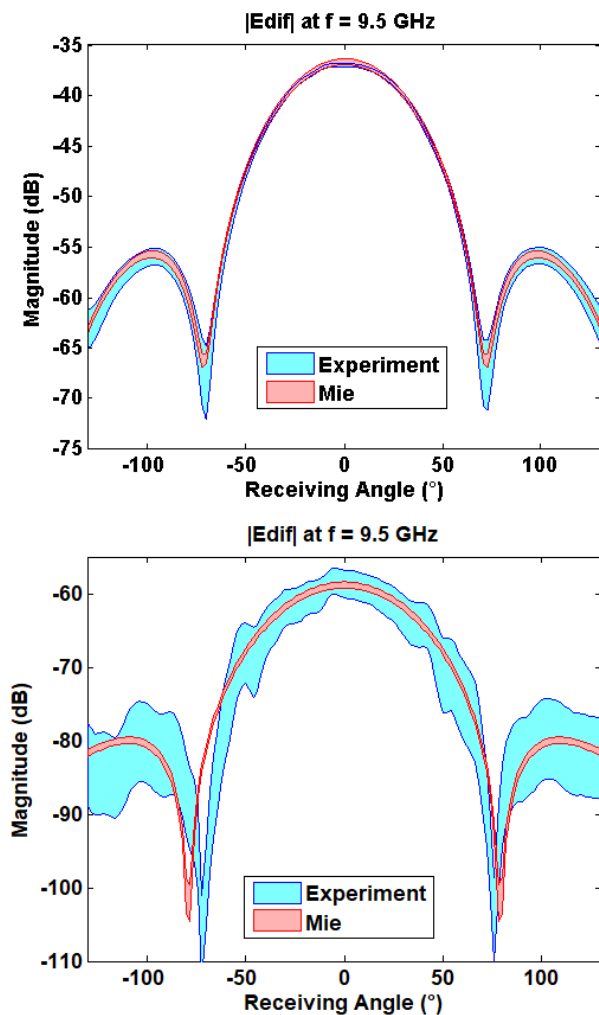

Fig. 10. Representation of the uncertainty estimations for the $S_{1.39}$ sphere (top) and the $S_{1.03}$ sphere (bottom). The cyan zone represents the experimental scattered field with the standard deviation observed from 500 repetitive measurements. The light red zone represents the variations corresponding to a Monte-Carlo computation: 500 permittivity values taken from the extreme range values of permittivities are used as inputs to the Mie simulation.

Cross polarization measurements (VH) have also been made. In average, over all the measured angles, the cross-polar level stays about 20 dB under the co-polar level, indicating a small depolarization effect for all the spheres we have measured. The higher levels of cross-polar were measured at the highest frequency and for the longest cylinders, confirming thus that it can be interesting to shorten the cylinders as much as possible.

IV. CONCLUSION

In this work, we have proposed a methodology, which aims at controlling locally the permittivity of 3D printed objects. It consists in using a photocurable resin as a bulk material in

which non-uniform porosities are created and distributed in a non-structured way through a meshing scheme. Starting from the permittivity of the bulk material, the value of ε' can be decreased on demand by decreasing the material density in the objects, and this latter is adjusted by selecting the convenient length and diameter of the meshes edges.

Several spheres samples are manufactured with this technique with values of ε' between 1 and 2.5. The permittivity characterization is made through far field scattering measurement and comparison to Mie simulations. The manufacturing of high-resolution objects with cylinder diameter down to 0.2 mm was successfully achieved using a DLP 3D printer, with no observed printing defects or shrinking effects. It was also possible to measure the fields scattered by spheres with a high air volume, up to 90%, which make them very low scattering objects.

The good choice of the mesh/cylinder dimensions combination has also been investigated. These two parameters are scaled for different spheres of permittivities ranging between 2.3 and 2.5. It is shown that decreasing the mesh size enhances the global homogenization of the meshed object, but there are limits. The object is 3D printed inside a vat of liquid photosensitive polymer and the uncured liquid must flow out of the object after fabrication. For this reason, internal openings in the object need to be maintained. As a result, when the mesh size is reduced, the material quantity increases and this needs to be overcome by reducing the cylinders diameter. Other technologies, such as Fused Deposition Modeling technologies, might not suffer from such a limitation.

The proposed methodology, which has been made to be user independent as possible, could be used by designers of antennas, metamaterials and microwave components when no existing material satisfies their permittivity requirements.

REFERENCES

[1] Brakora, K.F., Halloran, J. and Sarabandi, K., 2007. Design of 3-D monolithic MMW antennas using ceramic stereolithography. IEEE transactions on antennas and propagation, 55(3), pp.790-797.

[2] Liang, M., Ng, W.R., Chang, K., Gbele, K., Gehm, M.E. and Xin, H., 2014. A 3-D Luneburg lens antenna fabricated by polymer jetting rapid prototyping. *IEEE Transactions on Antennas and Propagation*, *62*(4), pp.1799-1807.

[3] Larimore, Z., Jensen, S., Parsons, P., Good, B., Smith, K. and Mirotznik, M., 2017. Use of space-filling curves for additive manufacturing of three dimensionally varying graded dielectric structures using fused deposition modeling. Additive Manufacturing, 15, pp.48-56.

[4] Wu, Z., Kinast, J., Gehm, M.E. and Xin, H., 2008. Rapid and inexpensive fabrication of terahertz electromagnetic bandgap structures. Optics express, 16(21), pp.16442-16451.

[5] R. C. Rumpf, J. Pazos, C. R. Garcia, L. Ochoa, and R. Wicker. (2013). 3D Printed Lattices with Spatially Variant Self-Collimation. *Prog. Electromagn. Res.* [Online]. *139,* pp. 1–14. Available: http://www.jpier.org/PIER/pier.php?paper=13030507

[6] C. R. Garcia, J. Correa, D. Espalin, J. H. Barton, R. C. Rumpf, R. Wicker, and V. Gonzalez. (2012). 3D Printing of Anisotropic Metamaterials. *Prog. Electromagn. Res. Lett.* [Online]. *34,* pp. 75–82. Available: http://www.jpier.org/PIERL/pier.php?paper=12070311

[7] B. Ratni, J. Yi, X. Ding, A. de Lustrac, K. Zhang, G-P. Piau, and S. N. Burokur. (2018). Gradient phase partially reflecting surfaces for beam steering in microwave antennas. *Opt. Express.* [Online]. *26 (6),* pp. 6724–6738. Available: https://www.osapublishing.org/oe/abstract.cfm?uri=oe-26-6-6724

[8] F. Castles, D. Isakov, A. Lui, Q. Lei, C.E.J. Dancer, Y. Wang, J.M. Janurudin, S.C. Speller, C.R.M. Grovenor, and P.S. Grant. (2016). Microwave dielectric characterisation of 3D-printed BaTiO3/ABS polymer composites. Sci. Rep. [Online]. 6. Available: https://www.nature.com/articles/srep22714

[9] M. Yin, X. Y. Tian, L. L. Wu, and D. C. Li. (2013). A Broadband and omnidirectional electromagnetic wave concentrator with gradient woodpile structure. Opt. Express. [Online]. 21 (16), pp. 19082-19090. Available: https://www.osapublishing.org/oe/abstract.cfm?uri=oe-21-16-19082

[10] N. Delhote, S. Bila, D. Baillargeat, T. Chartier, and S. Verdeyme. (2011). "Advanced design and fabrication of microwave components based on shape optimization and 3D ceramic stereolithography process," in *Advances in Ceramics-Synthesis and Characterization, Processing and Specific Applications*. *Intech.* Available:

[11] N. T. Nguyen, N. Delhote, M. Ettorre, D. Baillargeat, L. L. Coq, and R. Sauleau, "Design and Characterization of 60-GHz Integrated Lens Antennas Fabricated Through Ceramic Stereolithography," *IEEE Trans. Antennas Propag.*, vol. 58, no. 8, pp. 2757–2762, Aug. 2010

[12] N. Delhote, D. Baillargeat, S. Verdeyme, M. Thevenot, C. Delage, and C. Chaput. "Large experimental bandpass waveguide in 3D EBG woodpile manufactured by layer-by-layer ceramic stereolithography," in *IEEE/MTT-S International Microwave Symposium.*, Honolulu, HI, 2007, pp. *1431.*

[13] N. Delhote, D. Baillargeat, S. Verdeyme, C. Delage, and C. Chaput. (2007). Innovative Shielded High Q Dielectric Resonator Made of Alumina by Layer-by-Layer Stereolithography. *IEEE Microw. Wirel. Compon. Lett.* [Online]. *17 (6),* pp. 433–435. Available: https://ieeexplore.ieee.org/document/4220697

[14] R. Vaillon, J.M. Geffrin, Recent advances in microwave analog to light scattering experiments, J. Quand. Spectrosc. Radiat. Transf [Online] 146, pp. 100-105, 2014. Available: https://www.sciencedirect.com/science/article/abs/pii/S0022407314000880

[15] O. Merchiers, C. Eyraud, J.M. Geffrin, R. Vaillon, B. Stout, P. Sabouroux, B. Lacroix. (2010). Microwave measurements of the full amplitude scattering matrix of a complex aggregate: a database for the assessment of light scattering codes. *Opt. Express.* [Online]. *18 (3),* pp. 2056-2075. Available: https://www.ncbi.nlm.nih.gov/pubmed/20174035

[16] Á. I. Barreda, H. Saleh, A. Litman, F. González, J.M. Geffrin, and F. Moreno. (2017). Electromagnetic polarization-controlled perfect switching effect with high-refractive-index dimers and the beam-splitter configuration. *Nat. Commun.* [Online]. *8,* pp. 13910. Available: https://www.nature.com/articles/ncomms13910

[17] H. Saleh, J. Charon, J. Dauchet, H. Tortel, and J. M. Geffrin. (2017). Microwave analog experiments on optically soft spheroidal scatterers with weak electromagnetic signature. *J. Quant. Spectrosc. Radiat. Transf.* [Online]. *196,* pp. 1-9, 2017. Available: https://www.sciencedirect.com/science/article/pii/S0022407317300353

[18] *C. Geuzaine and J.F. Remacle. (2009). Gmsh: A 3-D finite element mesh generator with built-in pre- and post-processing facilities. Int. J. Numer. Methods Eng. [Online]. 79 (11). Available:* https://onlinelibrary.wiley.com/doi/abs/10.1002/nme.2579

[19] *"CATIA". https://www.3ds.com/fr/produits-et-services/catia/*

[20] C. Eyraud, J. M. Geffrin, A. Litman, and H. Tortel. (2015). Complex Permittivity Determination From Far-Field Scattering Patterns. *IEEE Antennas Wirel. Propag. Lett.* [Online]. *14,* pp. 309-312. Available: https://ieeexplore.ieee.org/document/6922486

[21] C. Eyraud, A. Litman, A. Hérique, and W. Kofman. (2009). Microwave imaging from experimental data within a bayesian framework with realistic random noise. *Inverse Problems.* [Online]. *25 (2).* Available: http://iopscience.iop.org/article/10.1088/0266-5611/25/2/024005

[22] J.M. Geffrin and P. Sabouroux. (2009). Fresnel database continuation: Experimental setup and improvements for 3d scattering measurements. *Inverse Problems.* [Online]. Available: http://iopscience.iop.org/article/10.1088/0266-5611/25/2/024001

[23] C. Eyraud, J.M. Geffrin, A. Litman, P. Sabouroux and H. Giovannini. (2006). Drift correction for scattering measurements. *Appl. Phys. Lett.* [Online]. *89*. Available: https://aip.scitation.org/doi/10.1063/1.2404978

[24] C. F. Bohren, D. R. Huffman, and Z. Kam. (1983). Book-Review - Absorption and Scattering of Light by Small Particles. *Nature*. *306*, pp. 625.

[25] H. Saleh, "Application of the Microwave Analogy to Study the Scattering Properties of Trees, Atmospheric Particles and Microorganisms," PhD thesis, Aix-Marseille university, 2017